Analysis of Field-Driven Clocking for Molecular Quantum-Dot Cellular Automata Based Circuits

F Karim, K Walus and A Ivanov

University of British Columbia, Department of Electrical and Computer Engineering, 2332 Main Mall, Vancouver, BC, Canada V6T 1Z4

E-mail: {faizalk,konradw,ivanov}@ece.ubc.ca

Abstract. Molecular quantum-dot cellular automaton (QCA) offers an alternative paradigm for computing at the nano-scale. QCA circuits require an external clock which can be generated using a network of submerged electrodes to synchronize information flow and provide the required power to drive the computation. In this paper, the effect of electrode separation and applied potential on the likelihood of different QCA cell states of molecular cells located above and in between two adjacent electrodes is analyzed. Using this analysis, estimates of operational ranges are developed for the placement, applied potential, and relative phase between adjacent clocking electrodes to ensure that only those states that are used in the computation are energetically favorable. Conclusions on the trade-off between cell size, cell-to-cell distance, and applied clocking potential are drawn and the temperature dependence of the operation of fundamental QCA building blocks is considered.

1. Introduction

Molecular quantum-dot cellular automaton (QCA) is an emerging nano-scale computing paradigm which utilizes the electrostatic coupling between electronic configurations in neighboring molecules to perform information processing. This computing paradigm was originally introduced by C. S. Lent [1] and has been extended in recent years to devices based on single molecules [2–9]. Several proof-of-concept QCA devices have been fabricated using silicon-on-insulator (SOI) [10], metallic island implementations operating in the Coulomb blockade regime [11–17], and nano-magnetics [18–23]. Recently, work by Haider *et al.* has demonstrated room temperature operation of an atomic-scale QCA cell using coupled Si dangling bonds [24]. A simulation tool exists for this technology [25–28] and has been applied towards the high-level design and exploration of both sequential and combinational circuits [29–31].

A clocking implementation using submerged electrodes to generate an electric field at the level of the QCA molecules was initially proposed in [32]. While this type of clocking has generated considerable interest in recent years [5, 33, 34], the *design* parameters of such clocking electrodes have not been fully addressed. This paper investigates the design of the clocking infrastructure required for molecular QCA implementations. We develop limits on the clocking potential and maximum phase difference of adjacent electrodes to ensure error free operation. In the final section of this paper, we investigate the temperature dependence of these building blocks and estimate RMS voltages required to clock the circuit. This work provides tools to analyze the total power to determine the contribution that can be expected from the clocking network.

2. 3-State QCA

The fundamental unit in QCA is the QCA cell, created with either 4 or 6 quantum dots and 2 mobile electrons. A molecular implementation of QCA cells could offer several advantages over its metal and magnetic counterparts. Firstly, if we consider a molecular QCA cell as a single-molecule device, then QCA circuits can achieve device densities on the order of $10^{14}/\text{cm}^2$ (for 1 nm^2 devices) [6]. The power dissipated from current-switched devices such as FETs operating at GHz speeds could melt the chip at those densities [35], however molecular QCA has been predicted to reduce the power dissipation by several orders of magnitude [36,37]. Additionally, the smaller the size, the larger the interaction energies between the cells. At the molecular scale, these energies are expected to be in the 0.2-0.5 eV range [1, 38, 39] which allow for room temperature operation since these energies are greater than the thermal ambient energy (*i.e*, thermal noise) k_BT ($\sim$25 meV at room temperature), where k_B is Boltzmann's constant and T is the temperature in kelvin ($T = 293$ K at room temperature). Lastly, molecular QCA can be clocked at very high frequencies (adiabatically at 1 THz) [36] - much faster than reported speeds of the magnetic QCA cell [39].

3. Model

In a molecular implementation, the role of quantum dots is played by redox centers within the molecule. A redox center can gain an electron (*i.e.*, be reduced) or lose an electron (*i.e.*, be oxidized) without breaking chemical bonds [5, 9]. In particular, two types of redox centers have been investigated - those whose non-bonding orbitals are comprised of mainly s and p states and those whose states are principally comprised of d states from transition metals [2, 4, 5]. Si-pthalocynanine is an example of the former [40] while an example of the latter is the Ru-based Creutz-Taube ion [41]. The advantage of the latter is that these metal organic compounds can be stable ions for much longer, while the former tend to be very reactive.

In the context of this paper, a simplified model of a molecular QCA cell based on a structure similar to [42, 43] is investigated in order to reduce the model complexity so that a set of analytical expressions to describe the effect of the clocking electrodes on the ground state of the molecular QCA cell can be developed. A full quantum mechanical model using *ab initio* simulations has been studied by Lu *et al.* [42–44] and demonstrates that this simplified model is able to accurately predict the switching behavior of these molecular cells. Here, we use a 3-dimensional QCA cell geometry which includes a mechanism for clocking molecular QCA cells proposed in [5, 33, 34], and has been shown to act as a QCA device, switching from a chemical representation of a binary 0 to a binary 1. In this work, the dynamics of these cells are not considered. Instead, only the ground state energies of different circuit configurations and applied clocking bias are determined. The aim of this work is to use these energies to derive the relationships that exist between the cell size, cell-to-cell distances and applied clocking potentials. In their simplified form, the 3-state QCA cells are composed of "V"-shaped molecules, each with three redox sites, grouped in pairs. Each pair of molecules represents an individual QCA cell as shown in Figure 1. Here, the three basis states of a QCA cell are shown. The redox sites represent locations in the molecule where the mobile charges can exist and play the role of the quantum dots. Spin and other internal degrees of freedom such as mechanical vibration or deformations due to Coulombic forces are not considered in this work. Furthermore, while it is expected that chemical conformation will play a role in the behavior of molecules and should be studied further, it is not explicitly considered in this paper as it is beyond the scope of this work. However, it should be noted that chemical conformations in mixed-valence systems do not provide any significant geometric effects [45].

For the molecular QCA cell, three stable electronic configurations are chosen as a basis. Two electronic configurations, in which the mobile charges are located in the top sites of the cell and along one of the two diagonals, represent the ACTIVE states of the cell. In these ACTIVE configurations, the cell is said to have a polarization, $P = \pm 1$. When $P = 1$, the cell is said to represent a binary value of 1, and when $P = -1$, the cell is said to represent a binary value of 0 as shown in Figure 1. When a cell is in one of the two ACTIVE states, its electrostatic interaction with neighboring cells introduces a

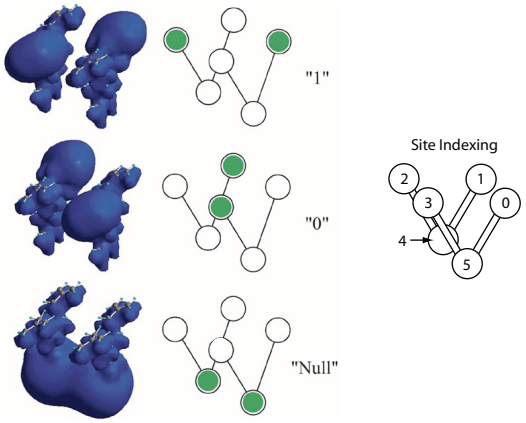

Figure 1. 3-state QCA cells are composed of "V"-shaped molecules grouped in pairs [46]. The site indexing used throughout this paper is indicated in the right figure. Reproduced with permission (© 2003 IEEE).

perturbation that breaks the energy degeneracy of the active states of the neighboring cells and in the ground state configuration, adjacent cells tend to relax to the same ACTIVE state. In the NULL state, where the cell has a polarization, $P = 0$, the mobile charges are located in the bottom sites of the cell. In this configuration, the cell does not break the energy degeneracy of ACTIVE states in neighboring cells. Therefore, cells relax to a polarization that is determined only by neighboring cells for which $P \neq 0$, and this provides a mechanism for turning cells "off."

A schematic diagram of a QCA cell is shown in Figure 2 depicting the different polarizations of the cell. For simplicity, the bottom two sites are not shown. Here, the bounding box around the cell is used only to distinguish one cell from another and has no physical analogue.

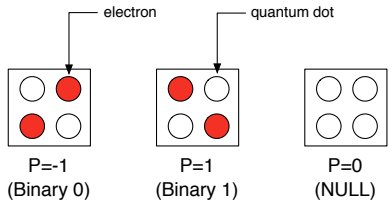

Figure 2. Three QCA cells with different polarizations are shown. Each cell carries two extra electrons which tend to occupy the diagonals of the cell when in one of the two ACTIVE states.

3.1. Charges

Two fixed positive charges are placed underneath the cell to represent the counter-ion and ensure that the system is charge-neutral. The location of the neutralizing positive charge is determined by the parameter, d_c, and is shown in Figure 3.

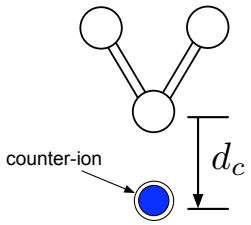

Figure 3. Location of the counter-ion charge in a 3-dot half-cell.

The total charge at each site of a cell and at the location of the counter-ions for the three basis states is

$$Q_+ = [-e, 0, -e, 0, 0, 0, e, e]^T, \tag{1}$$

$$Q_- = [0, -e, 0, -e, 0, 0, e, e]^T, \tag{2}$$

and

$$Q_{NULL} = [0, 0, 0, 0, -e, -e, e, e]^T, \tag{3}$$

where e is the charge of an electron. The elements of these charge vectors (including the counter-ions, CI) are

$$Q = \left[Q_{\text{site }0}, Q_{\text{site }1}, Q_{\text{site }2}, Q_{\text{site }3}, Q_{\text{site }4}, Q_{\text{site }5}, \text{CI}_1, \text{CI}_2\right]^T, \tag{4}$$

with respect to the indexing shown in Figure 1 and counter-ion location in Figure 3.

4. Clocking

Clocking is required in order to synchronize information flow in a QCA circuit. It is also required to deliver power to run the circuit [36]. Clocking can be implemented with a set of submerged electrodes that generate an electric field at the level of the QCA molecules [32]. The application of phase shifted sinusoids to each of the electrodes creates a traveling wave and induces a different electric potential at each of the different sites of the cell. As a result of the electric fields, cells are forced to switch states at the wavefront of this forward moving wave as illustrated in Figure 4. Here, the signal applied to each of the four electrodes shown in Figure 4 is shifted by ϕ_i as indicated on the electrodes, such that $\phi_1 < \phi_2 < \phi_3 < \phi_4$.

When the applied electric field on the cell in the $\hat{y}$ direction, E_y, is sufficiently large, it will draw the mobile electrons towards the bottom two sites of the cell forcing the cell into the NULL state. Conversely, if the applied field is reversed, it will drive the electrons to the upper sites of the cell and force it into one of the ACTIVE states. If the field is only somewhat positive or negative, the cell will be in a switching state, partially occupying both the upper and lower sites of the cell. Which of the cell's upper sites are occupied is not determined by the electric field in the $\hat{y}$ direction, but instead by the quadrupole-quadrupole interactions between neighboring cells which determine whether a logic "1" or a logic "0" is energetically favorable. Note that it is also possible

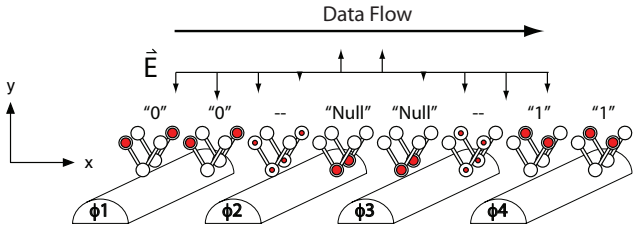

Figure 4. Submerged electrodes can be used to clock QCA cells by generating a forward moving electric field at the level of the cells. A ground plane located above the cells is not shown in the figure. The sizes of the QCA cells shown here are not to scale with respect to the spacing of the electrodes, and many real cells can be placed between adjacent electrodes.

to implement a QCA cell using two mobile holes instead of electrons. In this case, only the direction of the electric field would be reversed.

5. Configuration Energies

Intracellular electrostatic energies are calculated using the standard formula,

$$U_{\kappa}^{intra} = \frac{1}{4\pi\epsilon_0\epsilon_{r_1}} \sum_{i=0}^{6} \sum_{j=i+1}^{5} \frac{Q_{\kappa}(i)Q_{\kappa}(j)}{|r(i) - r(j)|} \tag{5}$$

where $\kappa = \{+, -, NULL\}$ represents one of the three underlying configurations. The distance between the upper adjacent sites, *i.e.*, sites 0-3, is d; diagonal site separation is therefore, $\sqrt{2}d$. Sites 4 and 5 are located a distance h below the plane of a cell's upper sites. For the purposes of this work, the cell size is defined as the inter-site distance, d. An illustration of the QCA cell dimensions is shown in Figure 5.

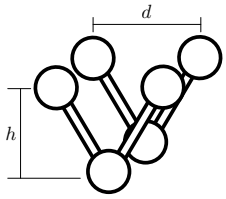

Figure 5. QCA cell dimensions.

The electrostatic potential induced by neighboring cells is computed using,

$$V_{\kappa_m}^{m}(i) = \frac{1}{4\pi\epsilon_0\epsilon_{r_1}} \sum_{j=0}^{5} \frac{Q_{\kappa_m}^{m}(j)}{|r(i) - r^m(j)|}, \tag{6}$$

where $V_{\kappa_m}^{m}(i)$ is the potential at the i^{th} site due to neighboring cell m in basis state κ, $Q_{\kappa_m}^{m}$ is the charge vector of cell m, and $r^m(j)$ is distance to the j^{th} site of cell m. Using

equation (6), an expression for the interaction energies between cells n and m can be described by the following [47, 48],

$$U^{inter}_{\kappa_n,\kappa_m} = \sum_{m \in \mathbf{N}_c} \sum_{i=0}^{5} Q_{\kappa_n}(i) V^m_{\kappa_m}(i), \tag{7}$$

where $\mathbf{N}_c$ is the effective neighborhood of cell n and is defined here as all cells existing within a single cell radius of n. Here, κ_n and κ_m represent the basis states for cells n and m, respectively.

6. Electrodes

In this work, only two adjacent electrodes are considered and the energetics of a single cell located directly above the mid-point between the electrodes is modeled. This case is considered because the applied potential of the electrodes has the least effect on the middle cell and thus making it the most difficult cell to switch between the ACTIVE and NULL states. As well, the transverse component of the electric field is strongest at this point and it is shown in Section 8.2 that a very strong transverse field can drive the cell into unwanted states. The clocking electrodes are buried in an oxide and are modeled as thin conducting wires of radius a, whose potentials are measured relative to a ground plane located above the layer of cells as shown in Figure 6.

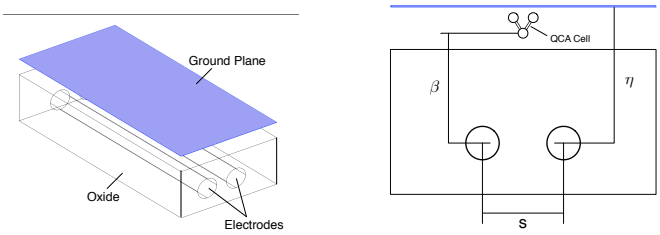

(a) Perspective View (b) Cross-Section

Figure 6. Perspective and cross-sectional view showing the location of the two modelled electrodes, ground plane and the QCA cell. The size of the QCA cell is not to scale with respect to the spacing of the electrodes.

We also define two important quantities that are used throughout the remainder of the paper. The first is the average electrode potential,

$$V_{avg} = \frac{V_{e_1} + V_{e_2}}{2}, \tag{8}$$

and the second is the electrode potential difference,

$$\Delta V_e = V_{e_2} - V_{e_1}, \tag{9}$$

where V_{e_1} and V_{e_2} are the potentials on two adjacent electrodes.

6.1. Clocking Energies

The overall electrostatic energy of the cell configuration due to the clocking electrodes is

$$U_{\kappa}^{clk} = \sum_{i=0}^{5} V_{clk}(i) Q_{\kappa}(i), \tag{10}$$

where V_{clk} is the induced potential at each of the sites of the cell due to the clocking electrodes. If the distance between neighbouring electrodes is much larger than the size of the cells, *i.e.*, $s \gg d$, then it can be assumed that E_y is nearly uniform across the cell and the overall electrostatic energy difference between the ACTIVE and NULL cell configurations due the clocking electrodes can be approximated as

$$\Delta U_{NA}^{clk} = -2heE_y. \tag{11}$$

E_y was calculated by using COMSOL 3.3 which modeled two adjacent electrodes, spaced 20 nm to 110 nm apart, and the electric field data produced after each simulation was recorded. The corresponding average electrode potential, V_{avg}, and potential difference, ΔV_e, used to generate the electric field for each electrode spacing was also extracted. Figure 7 shows the field graph from one of the COMSOL simulations. Identical 5V sinusoids were applied to each electrode, which were embedded in a substrate with a dielectric constant of 4.2. The arrows in the figure indicate the magnitude and direction of the electric field. The color map is used to represent the potential in the system.

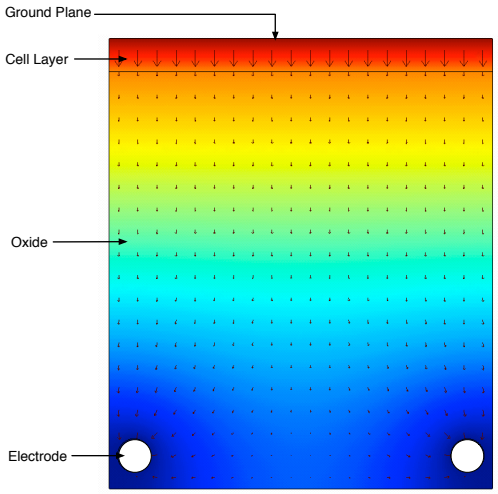

Figure 7. An electric field graph from a COMSOL simulation. The dielectric constant of the oxide was chosen to be 4.2. Identical 5V sinusoids were applied to each electrode.

Due to the orientation of the molecular cell, the application of this clocking field does not introduce any bias between the two ACTIVE states. However, the clock will introduce an energy difference between the NULL and ACTIVE states, permitting it to be used to switch the cell between the ACTIVE and NULL states.

7. 3-Dot Cell

In [42, 43], the authors conduct a high-level *ab initio* CASSCF calculation on the single 3-dot half cell consisting of a cationic 1,10,19-eicosatriene molecule shown in Figure 8. In those works, the authors show that it is possible to capture the relevant switching behavior of this molecule by constructing the following 3-state Hamiltonian for the cell,

$$\hat{H} = \begin{bmatrix} E_0 - e\epsilon d/2 & -\gamma & 0 \\ -\gamma & E_0 + E_c & -\gamma \\ 0 & -\gamma & E_0 + e\epsilon d/2 \end{bmatrix}, \tag{12}$$

where E_0 is the on-site energy of each state, E_c is the energy provided by the clock, and ϵ is the switching field from neighboring molecules. d and γ are the effective distance and tunneling energy between the central and edge dots. Cell dimensions for this molecule are shown in Figure 9. It can be shown that our simplified model (described in equations (5)-(11)) can be used to predict the diagonal elements of this Hamiltonian.

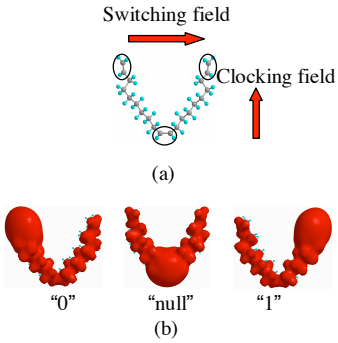

Figure 8. 3-dot, 3-state QCA cell described in [42, 43]. Reproduced with permission (© 2007 American Institute of Physics).

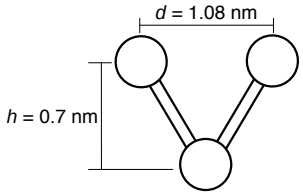

Figure 9. Cell dimensions for the 3-dot cell simulated in [42, 43].

The three energies corresponding to the ACTIVE and NULL states found from using the simple three-state Hamiltonian are in excellent agreement with those found using the more rigorous *ab initio* CASSCF calculations, and as such, provide basic justification for our choice of model.

8. Analysis of Configuration Energies

In this section, we analyze the electrostatic energy of the different possible configurations of a cell placed directly above the mid-point between two identical electrodes to determine its dependence on the various cell parameters. The maximum phase difference between neighboring electrodes is also discussed. The equations developed here will be used in the later sections of this work to determine the minimum electrode potentials required to switch a cell between the ACTIVE and NULL states, as well as to predict limits on the relative phase between adjacent electrodes.

8.1. ACTIVE to NULL

Here, we analyze the energy of a single cell in the ACTIVE and NULL states. The total electrostatic energy for the ACTIVE and NULL states is given by

$$\begin{aligned} U_{ACTIVE} &= U^{intra}_{ACTIVE} + U^{clk}_{ACTIVE} + U^{inter}_{ACTIVE,\kappa_m}, \\ U_{NULL} \quad &= U^{intra}_{NULL} + U^{clk}_{NULL} + U^{inter}_{NULL,\kappa_m}. \end{aligned} \tag{13}$$

We are interested in the difference between these two energies; *i.e.*,

$$\begin{aligned} \Delta U_{NA} &= U_{NULL} - U_{ACTIVE} \\ &= \Delta U^{intra}_{NA} + \Delta U^{clk}_{NA} + \Delta U^{inter}_{NA}. \end{aligned} \tag{14}$$

From the above, it follows that when ΔU_{NA} is positive, the cell will tend to the ACTIVE state since it represents the lower energy state, and when negative, to the NULL state. Using equation (5), the ΔU^{intra}_{NA} term can be expressed as

$$\Delta U^{intra}_{NA} = e^2 \frac{\left(\frac{\sqrt{2}-2}{4d} - d_c^{-1} + \gamma_1^{-1} + \gamma_2^{-1} + \gamma_3^{-1}\right)}{2\pi\epsilon_0\epsilon_{r_1}}, \tag{15}$$

where the two γ_i terms can be constructed using

$$\begin{aligned} \gamma_1 &= \sqrt{d^2 + d_c^2} \\ \gamma_2 &= \sqrt{h^2 + \frac{5d^2}{4} + 2hd_c + d_c^2}, \\ \gamma_2 &= \sqrt{h^2 + \frac{d^2}{4} - 2hd_c + \frac{d_c^2}{4}}, \end{aligned}$$

where h is the cell height, d is the cell size and d_c is the distance between the bottom sites of the cell and the counter-ion. We will expand the ΔU^{inter}_{NA} term in later sections of this paper.

8.2. ACTIVE to X

The assumption that the cell will only exist in one of three underlying basis states requires that E_x, *i.e.*, the field across the cell, be sufficiently low so that the two mobile charges do not accumulate at one side of the cell. These higher energy states, sometimes

called "X" states, are shown in Figure 10. If cells are permitted to go into such states, data will be lost and the circuit will fail to operate properly. The following analysis is performed in order to define a maximum potential difference between adjacent electrodes to ensure that cells do not reach these unwanted states.

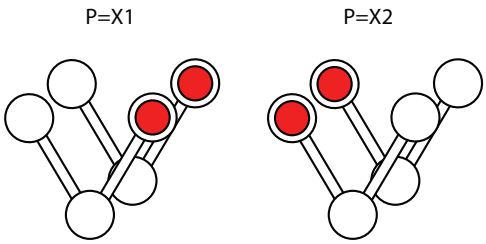

Figure 10. When the mobile charges are both located on the same side of the cell, the cell is said to be in one of the unwanted X states. These higher energy states can be avoided with proper design of the clocking electrodes.

The charge vectors associated with these two unwanted states are

$$Q_{X1} = [-e, -e, 0, 0, 0, 0, e, e]^T , \tag{16}$$

and

$$Q_{X2} = [0, 0, -e, -e, 0, 0, e, e]^T . \tag{17}$$

Whether or not the cell tends to one of these two states can be determined by first evaluating the difference in clocking energies for both the ACTIVE and X state, then adding this to the difference in their intra- and inter-cellular energies; *i.e.*,

$$\begin{aligned} \Delta U_{XA} &= U_{X_{1,2}} - U_{ACTIVE} \\ &= \Delta U_{XA}^{intra} + \Delta U_{XA}^{clk} + \Delta U_{XA}^{inter}. \end{aligned} \tag{18}$$

Using equation (5), ΔU_{XA}^{intra} can be expressed as

$$\Delta U_{XA}^{intra} = -e^2 \frac{(\sqrt{2}-2)}{8d\pi\epsilon_0\epsilon_{r_1}}. \tag{19}$$

8.3. Maximum Phase Difference

For a given configuration of clocking electrodes and cell geometry, the analysis in Sections 8.1 and 8.2 can be used to determine a range for the potential difference between adjacent electrodes, ΔV_e. This information can further be used to determine the maximum phase difference between neighbouring electrodes that ensures that the transverse electric field intensity does not cause the cell to relax into one of these unwanted states, which is expressed as,

$$\phi_{max} = \pm 2 \sin^{-1}\left(\frac{\Delta V_{e_{max}}}{2V_0}\right) \text{ radians}, \tag{20}$$

where V_0 is the peak potential of the sinusoid applied to the electrodes. A full derivation for equation (20) can be found in the appendix.

It is desirable to achieve 90° for ϕ_{max} so that the a standard 4 phase QCA clocking scheme can be used. The maximum phase difference is revisited in the discussion on the limits of the electrode potential difference, ΔV_e, in Section 9.1.2.

9. Analysis of Building Blocks

In this section, three basic layouts are analyzed in order to estimate operational ranges for the spacing, applied potential, and relative phase between adjacent electrodes at 0 K:

(i) A single QCA cell placed directly at the mid-point between two identical electrodes (see Figure 11(a));

(ii) A 3-cell wire with the middle cell placed at the mid-point between two identical electrodes (see Figure 11(b));

(iii) A 3-input majority gate with the middle cell placed at the mid-point between two identical electrodes (see Figure 11(c)).

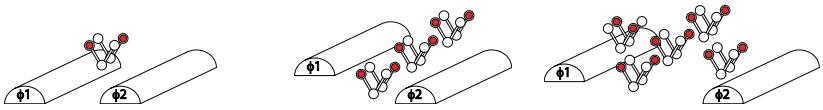

(a) Scenario 1 (b) Scenario 2 (c) Scenario 3

Figure 11. Considered layouts.

We choose these basic layouts because collectively, they form a set of fundamental building blocks from which any circuit can be built. For each plot, the value of d_c has been selected to be h unless otherwise specified, and the dielectric constants inside and between cells (ϵ_{r_1}) and in between the electrodes and molecules (ϵ_{r_2}) are chosen to be 1 and 4.2, respectively. The choice for ϵ_{r_2} (dielectric constant for SiO_2) is based on the assumption that the electrodes will be embedded in a silicon oxide as described in [49].

The ground plane was placed $\eta = 25$ nm above the electrodes as suggested in [32] for all layouts. To determine an optimal placement for the QCA cells, COMSOL 3.3 was used to find the height at which the ratio of the $\hat{y}$ directed electric field, E_y, above (E_{max_1}) and in between (E_{max_2}) the electrodes was closest to 1. This ratio is desirable since it represents the height above the electrodes at which E_y is most uniform. Higher ratios indicate the need for larger electrode potentials to meet the minimum field strength required to switch the cell from a NULL to an ACTIVE state. Figure 12 shows that this ratio approaches 1 as the cell elevation, β, is increased. Giving the increased uniformity of E_y as the cell elevation is increased, this result suggests that placing our

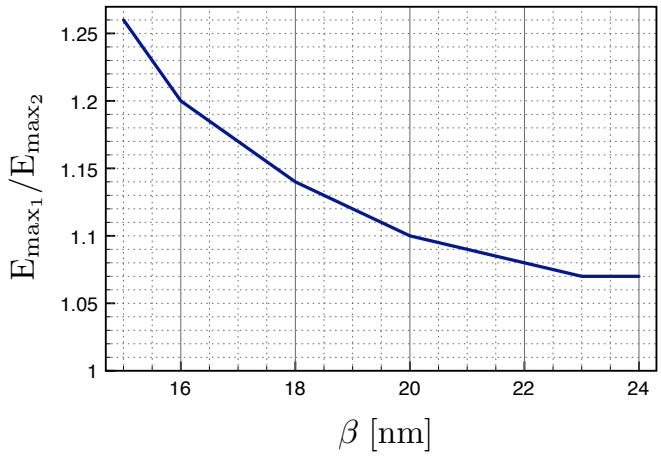

Figure 12. Ratio of the $\hat{y}$ directed electric field, E_y, above (E_{max_1}) and in between (E_{max_2}) the electrodes versus the cell elevation, β.

cells as high above the electrodes as possible will likely result in lower potentials being required to switch a cell from a NULL to ACTIVE state.

Both the ΔU_{NA}^{intra} and ΔU_{NA}^{clk} terms will remain unchanged for all three layouts since we are only modifying the arrangement of the neighboring cells in each layout; the cell of interest remains at a fixed position and will experience the same clocking field.

9.1. Single Cell

9.1.1. ACTIVE to NULL In the first layout, we considered a single cell with size $d = 1$ nm and a cell height of $h = 1$ nm [42, 43] placed $\beta = 23$ nm above the electrodes. The electrode length, l, and radius, a, were chosen to be 100 nm and 5 nm, respectively [50,51]. Here, we also apply the same potential to both electrodes, *i.e.*, $\Delta V_e = 0$. Equation (14) is solved for the electric field intensity, E_y, at which the cell is switched from an ACTIVE to a NULL state (or vice-versa), *i.e.*, when $\Delta U_{NA} = 0$. The corresponding average electrode potential, V_{avg}, is plotted for three values of d_c as a function of the electrode spacing, s, in Figure 13. V_{avg} for a molecule with no counter-ion is also shown.

The increase in switching potential as the electrode spacing is increased is expected. However, Figure 13 also shows that there exists a value of d_c such that the switching potential is 0 V, *i.e.*, a position of the counter-ion such that the cell changes from being normally NULL to being normally ACTIVE. This behavior is further illustrated in Figure 14, which plots V_{avg} against d_c for 3 different electrode spacings, s. For small d_c ($d_c < 3.25$ nm), the counter-ion pulls the mobile charges down - making the cell normally NULL. For large d_c, the larger charge separation between the active sites and the counter-ion make the cell change to being normally ACTIVE.

The cell size has significant impact on the switching potential of the clocking electrodes. Figure 15 shows the change in V_{avg} as the distance between adjacent electrodes is increased for five different cell sizes. From the figure, we see that the

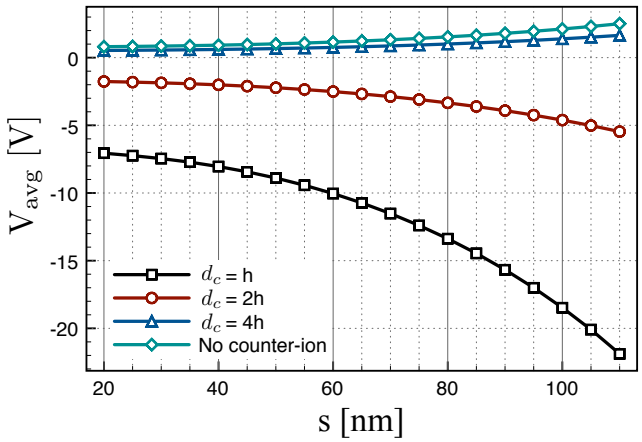

Figure 13. Switching potential versus electrode spacing for 3 different values of d_c for a 1 nm cell. The switching potential for a cell without a counter-ion is also shown.

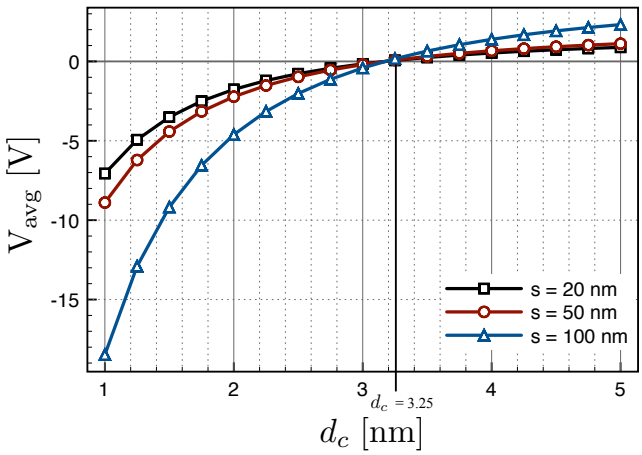

Figure 14. Switching potential versus d_c for a 1 nm cell. For $d_c > 3.25$ nm, the cell goes from being normally NULL to being normally ACTIVE.

switching potential increases as we decrease the cell size. This is expected since the clock needs to overcome the increased contribution from intracellular energies due to the increased proximity of the mobile electrons in the cell.

9.1.2. ACTIVE to X In the following analysis, the values of d, h and η as well as the electrode dimensions were kept the same as they were for the first layout. Since a strong $\hat{x}$-directed electric field is required to force a cell into one of the X states, a uniform electric field across the cell can no longer be assumed and hence, equation (10) must be used explicitly to compute the clocking energy of the cell. COMSOL 3.3 was used to find the potential induced at each of the sites due to the clocking electrodes and then multiplied by the charge vectors associated with the two X states. The maximum potential difference between the electrodes, ΔV_e, such that the middle cell does not go into an X state was plotted against the cell elevation, β, for the single cell, wire, and

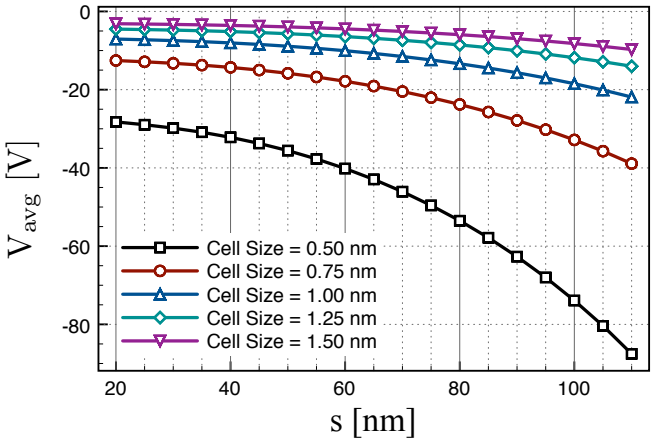

Figure 15. Switching potential for 0.5 nm, 0.75 nm, 1 nm, 1.25 nm and 1.5 nm cells as a function of the distance between adjacent clocking electrodes.

majority gate in Figure 16. A d_c value of h is used and the electrodes are spaced 20 nm apart. Figure 16 shows that as β increases, the maximum ΔV_e before the middle cell transitions from an ACTIVE to an X state also increased. For a single 1 nm cell placed $\beta = 23$ nm above the electrodes, 275 V would be required between neighbouring electrodes to drive the cell into an X state. If we consider that less than -20 V are required to switch the same cell from an ACTIVE to a NULL state (Figure 14), then this result suggests that X states are not likely to be a concern for small cells and will not require any additional design considerations. Furthermore, without any limits on the maximum ΔV_e, the maximum phase difference between neighboring electrodes also requires no design considerations.

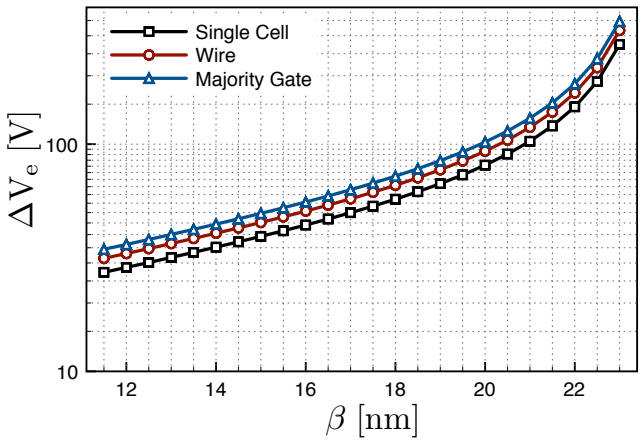

Figure 16. The maximum potential difference before the central cell is switched to an X state versus the cell elevation for a single cell, wire, and majority gate.

9.2. Wire

For the following layouts, we set up two different wire configurations as shown in Figs. 17(a) and 17(b). Figure 17(a) represents the worst-case scenario for forcing the middle cell into an ACTIVE state while Figure 17(b) represents the worst-case scenario for forcing the middle cell into the NULL state. The former case occurs as the cells are gradually being made ACTIVE. After the first two cells have switched into an ACTIVE state and the third cell begins to switch into the same ACTIVE state, it becomes energetically favorable for the middle cell to occupy the NULL state as a result of the extra charge present in the adjacent ACTIVE cells. This pattern is then repeated, creating a chain of alternating ACTIVE and NULL cells along the length of a wire. The same case occurs in the second configuration.

(a) Wire Configuration 1

(b) Wire Configuration 2

Figure 17. Wire configurations representing the maximum and minimum potentials for switching the middle cell. Cell indexing is shown in (a).

Figure 17(a) shows a cell sandwiched between two active cells, while Figure 17(b) shows the same cell in between two cells in the NULL state. For wire configuration 1 (w1), the interaction energy can be expressed as,

$$U^{inter_{(w1)}}_{NULL,ACTIVE} = \quad 2\sum_{i=0}^{5} Q^{n}_{NULL}(i)V^{n+1}_{ACTIVE}(i), \tag{21}$$

$$U^{inter_{(w1)}}_{ACTIVE,ACTIVE} = 2\sum_{i=0}^{5} Q^{n}_{ACTIVE}(i)V^{n+1}_{ACTIVE}(i) \tag{22}$$

The difference in state energies becomes,

$$\Delta U^{inter_{(w1)}}_{NA} = U^{inter_{(w1)}}_{NULL,ACTIVE} - U^{inter_{(w1)}}_{ACTIVE,ACTIVE}. \tag{23}$$

A full derivation for equations (21) and (22) can be found in the appendix. Similarly, the interaction energies for wire configuration 2 (w2) can be defined as,

$$U^{inter_{(w2)}}_{NULL,NULL} \quad = 2\sum_{i=0}^{5} Q^{n}_{NULL}(i)V^{n+1}_{NULL}(i), \tag{24}$$

$$U^{inter_{(w2)}}_{ACTIVE,NULL} = 2\sum_{i=0}^{5} Q^{n}_{ACTIVE}(i)V^{n+1}_{NULL}(i), \tag{25}$$

for which their energy difference becomes,

$$\Delta U_{NA}^{inter_{(w2)}} = U_{NULL,NULL}^{inter_{(w2)}} - U_{ACTIVE,NULL}^{inter_{(w2)}}. \tag{26}$$

Using equations (23) and (26) to calculate ΔU_{NA}^{inter} for wire configurations 1 and 2, respectively, Figure 18 plots equation (14) for both wire configurations, as a function of the average potential, V_{avg}, for cell size of 1 nm. All cell parameters are chosen to be the same as for the single cell layout with a cell-to-cell distance of 1 nm. From the graph, an average electrode potential of greater than -8 V is required to ensure that the cell is driven into the NULL state. Conversely, to ensure that the cell is ACTIVE, an average electrode potential below -11.3 V is required. This represents the minimum potential range that must be applied on each electrode to ensure the cell can be turned ACTIVE and NULL under all neighbor configurations.

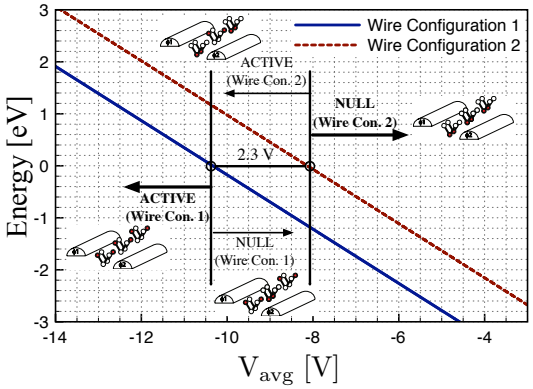

Figure 18. ΔU_{NA} plotted for both wire configurations using 1 nm cells. From the intercepts, it is shown that the applied potential range of the electrodes must be at least 2.3V for correct operation.

9.3. Majority Gate

Similar to the analysis of the wire, two different majority gate (MG) configurations in Figs. 19(a) and 19(b) that allow us to evaluate the maximum and minimum potential applied to the electrodes to ensure that the middle cell can be switched between the ACTIVE and NULL states.

MG configuration 1 (mg1) consists of a majority gate with two of its inputs and its output in the $P = +1$ state and the third input in the $P = -1$ state, while MG configuration 2 (mg2) has all three inputs and its output in the NULL state. As the middle and output cells of MG configuration 1 are being driven to the $P = +1$ state, it becomes energetically favorable for the middle cell to occupy the NULL state as a result of the extra charge in the upper-sites of the neighboring cells; thus configuration 1 presents the worst-case scenario for turning the middle cell "on." Moreover, for configuration 1, it should be noted that the order of the inputs does not matter, nor does the state of the opposing cell (*i.e.* a majority gate with two of its inputs in the $P = -1$

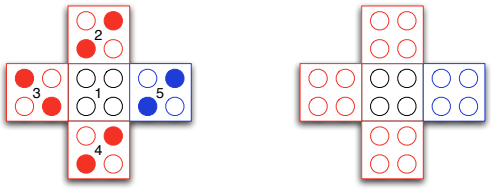

(a) MG Configuration 1

(b) MG Configuration 2

Figure 19. Majority gate configurations representing the worst-case scenarios for switching the middle cell. Cell indexing is shown in (a).

state and the third in the $P = +1$ state would yield the same results by symmetry). For MG configuration 1, the interaction energies can be expressed as,

$$\begin{aligned} U^{inter_{(mg1)}}_{NULL,\kappa_m} = 2\sum_{i=0}^{5} Q^1_{NULL}(i)V^2_+(i) \\ + \sum_{i=0}^{5} Q^1_{NULL}(i)V^3_-(i) \\ + \sum_{i=0}^{5} Q^1_{NULL}(i)V^5_+(i), \end{aligned} \tag{27}$$

$$\begin{aligned} U^{inter_{(mg1)}}_{ACTIVE,\kappa_m} = 2\sum_{i=0}^{5} Q^1_+(i)V^2_+(i) + \sum_{i=0}^{5} Q^1_+(i)V^3_-(i) \\ + \sum_{i=0}^{5} Q^1_+(i)V^5_+(i). \end{aligned} \tag{28}$$

The difference in state energies becomes,

$$\Delta U^{inter_{(mg1)}}_{NA} = U^{inter_{(mg1)}}_{NULL,\kappa_m} - U^{inter_{(mg1)}}_{ACTIVE,\kappa_m}. \tag{29}$$

A full derivation for equations (27) and (28) can be found in the appendix. Similarly, the interaction energies for MG configuration 2 can be written as,

$$U^{inter_{(mg2)}}_{NULL,\kappa_m} = 4\sum_{i=0}^{5} Q^1_{NULL}(i)V^2_{NULL}(i), \tag{30}$$

$$U^{inter_{(mg2)}}_{ACTIVE,\kappa_m} = 4\sum_{i=0}^{5} Q^1_{ACTIVE}(i)V^2_{NULL}(i), \tag{31}$$

such that their difference in energy becomes,

$$\Delta U^{inter_{(mg2)}}_{NA} = U^{inter_{(mg2)}}_{NULL,\kappa_m} - U^{inter_{(mg2)}}_{ACTIVE,\kappa_m}. \tag{32}$$

Using equations (29) and (32) to calculate ΔU^{inter}_{NA} for MG configurations 1 and 2, respectively, Figure 20 plots equation (14) for both majority gate configurations, as a

function of the average potential, V_{avg}, for cell size of 1 nm. The cell parameters are kept the same as in the previous analysis. It is apparent that the difference between the minimum and maximum electrode potentials is larger for the majority gate than that of the wire and is a result of the higher intercellular interaction of these configurations. For the same 1 nm cells, the minimum potential range increases from 2.3 V in the case of the wire to approximately 6.5 V for the majority gate. Thus, the minimum range of electrode potentials is determined by the majority gate and not the wire.

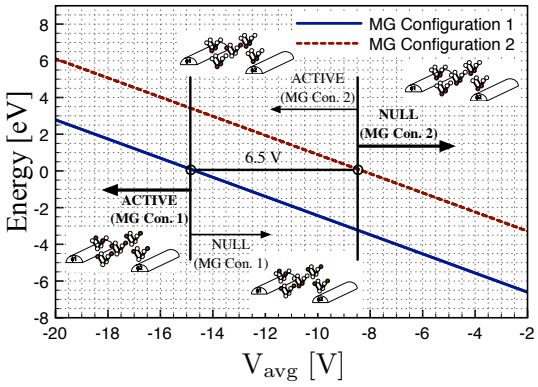

Figure 20. ΔU_{NA} plotted for both majority gate configurations using 1 nm cells. From the intercepts, it is shown that the applied potential range of the electrodes must be at least 6.5 V for correct operation.

For design purposes, it is important that we be able to determine *a priori* the minimum RMS voltage required by the electrodes since this will also be important in evaluating power dissipation in the clocking network. Let V_1 be the maximum allowable V_{avg} to keep the middle cell in MG configuration 1 in the ACTIVE state and V_2 be the minimum allowable V_{avg} to keep the cell in the NULL state for MG configuration 2. Then we can define V_{rms} as $\sqrt{(V_1^2 + V_2^2)/2}$. It is understood that this definition presents a pessimistic value for the RMS voltage as it can be reduced by setting $V_2 = 0$. Using this definition for the RMS voltage, a plot of V_{rms} as a function of the electrode spacing for five different cell sizes is shown in Figure 21. A second plot was produced comparing the effect of the intercellular distance on the RMS voltage for the majority gate in Figure 22. In the latter figure, it is shown that increasing the cell-to-cell distance decreases the minimum RMS voltage required for correct operation. This occurs because the inter-cellular energy of the majority gate decreases as the distance between cells is increased, and as such, the required switching potential from the electrodes is lowered.

This analysis can also be used to determine the minimum cell size for majority gates in order to satisfy certain layout conditions as shown in Figure 23. For instance, for a given RMS voltage and electrode spacing, one can use the results in Figure 23 to determine the smallest cell size allowed for correct operation of a majority gate.

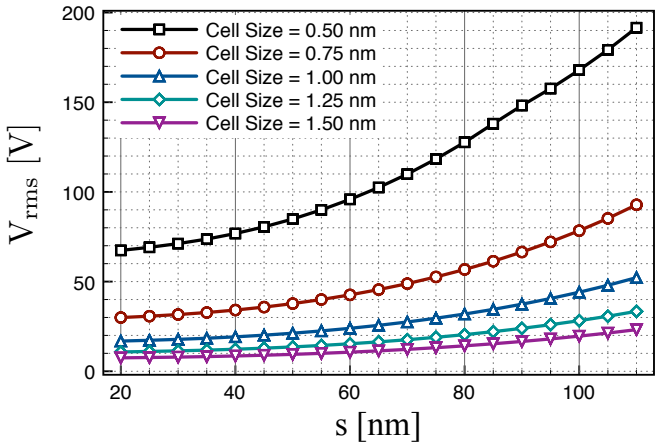

Figure 21. RMS voltage required by the electrodes for the majority gate for 0.5 nm, 0.75 nm, 1 nm, 1.25 nm, and 1.5 nm cells as a function of electrode spacing. $d_c = h$ used in all cases.

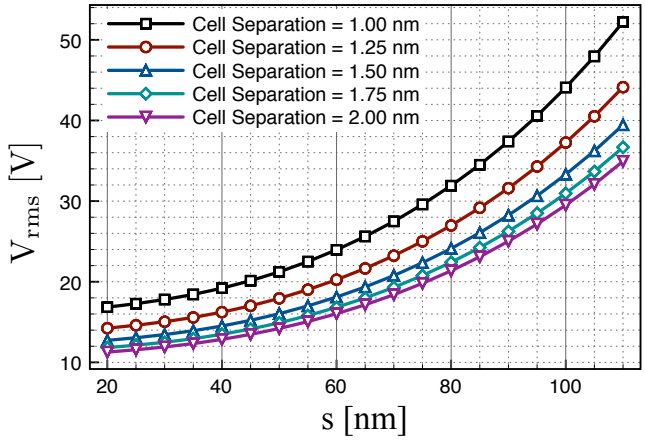

Figure 22. RMS voltage required by the electrodes for the majority gate as a function of electrode spacing, using a cell-to-cell separation of 1 nm, 1.25 nm, 1.50 nm, 1.75 nm and 2 nm. A cell size of 1 nm with $d_c = h$ was used in all cases.

10. Temperature Dependence

The preceding analysis assumed a temperature of 0 K. However, at finite temperature the thermodynamic effects must also be taken into consideration. The polarization of the cell is determined using the thermal expectation value of charge in each site and will depend on temperature. To account for this, a statistical thermodynamic model for a QCA cell is used [38, 52, 53]. Classically, a QCA circuit can be in one of many possible configurations, labelled, j, each with its associated total energy E_j. The expressions required to produce E_j have been developed in previous sections. Using the information of the possible states of the system, the canonical partition function in [38]

$$Z = \sum_j \exp\Big(\frac{-E_j}{k_B T}\Big), \tag{33}$$

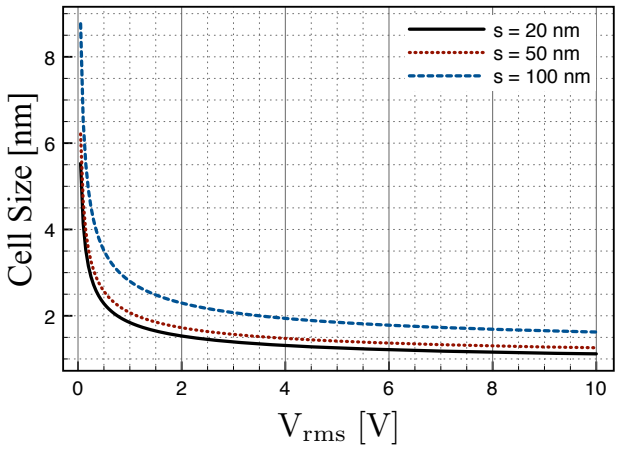

Figure 23. Minimum cell size required versus RMS voltage, V_{rms}, for 3 different electrode spacings. A cell elevation, $\beta = 23$ nm, is assumed with $d_c = h$.

can be used to compute the state probability for a particular configuration at a given temperature as

$$P_j = \frac{\exp(\frac{-E_j}{k_B T})}{Z}. \tag{34}$$

In the case of molecular QCA, where the thermal fluctuations are much faster than the measurement time, the thermal expectation value of charge in each site is computed using

$$\rho_i = P_+ Q_+(i) + P_- Q_-(i) + P_{NULL} Q_{NULL}(i). \tag{35}$$

The cell polarization can then be found by evaluating,

$$P = \frac{(\rho_0 + \rho_2) - (\rho_1 + \rho_3)}{\rho_0 + \rho_1 + \rho_2 + \rho_4 + \rho_5 + \rho_6}. \tag{36}$$

10.1. Cell to Cell Response

The non-linear cell-to-cell response function provides signal restoration in a QCA wire [44]. Figure 24 shows the cell-to-cell response between two neighboring 5 nm cells for three different operating temperatures. The switching potential, V, was chosen to be the minimum average electrode potential required to switch a 5 nm cell from an ACTIVE to a NULL state at 1K. As the driver's polarization is swept from $P_d = -1$ to $P_d = +1$, its neighboring cell takes on a polarization as determined by the driver. At increased temperature, the response function flattens as a result of the thermal fluctuations, which reduce the cell's ability to fully polarize. At 300K, Figure 24 shows that as $|P_d| \rightarrow 1$, the polarization of the driven cell is reduced. This occurs because as $|P_d| \rightarrow 1$, the amount of charge in the upper sites of the driver cell is increased, forcing the mobile charges in the driven cell towards the lower sites of the cell, allowing it to be partially in the NULL state as a result of thermal effects. The magnitude of

this effect depends on the switching potential. The ratio of charge in the active sites of the driven cell is also shown in Figure 24. It is clear from the figure that the less polarized the driver cell, the more charge that exists in the upper sites of the driven cell. As $P_d \to 0$, the quadrupole-quadrupole interaction between the cells is no longer strong enough to break the energy degeneracy of the ACTIVE states and thus, the driven cell's polarization goes to $P = 0$.

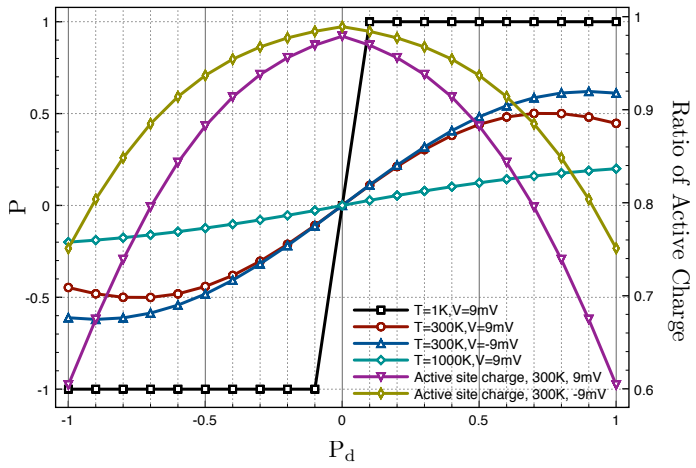

Figure 24. Cell-to-cell response function of two 5 nm cells for temperatures of 1K, 300K and 1000K. The ratio of total mobile charge in the active sites of the driven cell is also shown.

Lastly, Figure 24 shows that for appropriate switching potentials, as $P_d \to 0$, the slope of the response function is dependent only on temperature. The cell-to-cell response can be used to determine the maximum operating temperature of a given layout. In particular, we are interested in the temperature at which the slope of the response function at $P_d = 0$ drops below unity. For slopes below unity, the cell-to-cell interaction no longer provides signal restoration.

Figure 25 shows the temperature for the pair of cells described above, as well as for MG configuration 1 such that the slopes of their respective cell-to-cell response functions are unity. The electrode spacing, s, was kept at 20 nm, and all other cell parameters used were consistent with the previous analysis performed in this work. It is clear from this figure that the maximum operating temperature is limited by the pair of neighboring cells and not by the majority gate (or any other building block). The two neighboring cells present the case for which the interaction energies are the lowest and thus are the most sensitive to the increase in thermal fluctuations.

Using this maximum operating temperature, we can determine the minimum RMS voltage needed to switch the middle cell in the majority gate between the ACTIVE and NULL states. Recall, that it is the majority gate that determines the operational ranges of the clocking electrodes and not the wire. Once again, let V_1 be the maximum allowable V_{avg} to keep the middle cell in MG configuration 1 in the ACTIVE state and V_2 be the minimum allowable V_{avg} to keep the cell in the NULL state for MG configuration 2. Then

we can define V_{rms} as $\sqrt{(V_1^2 + V_2^2)/2}$. Using the maximum operating temperature, we can compute V_1 and V_2 by evaluating the required V_{avg} to drive a given fraction of the total mobile charge to the upper (ACTIVE) or lower (NULL) sites of the cells, thus turning them "on" or "off." Figure 25 shows the RMS voltages required to drive 90%, 75% and 50% of the mobile charge to the ACTIVE and NULL sites.

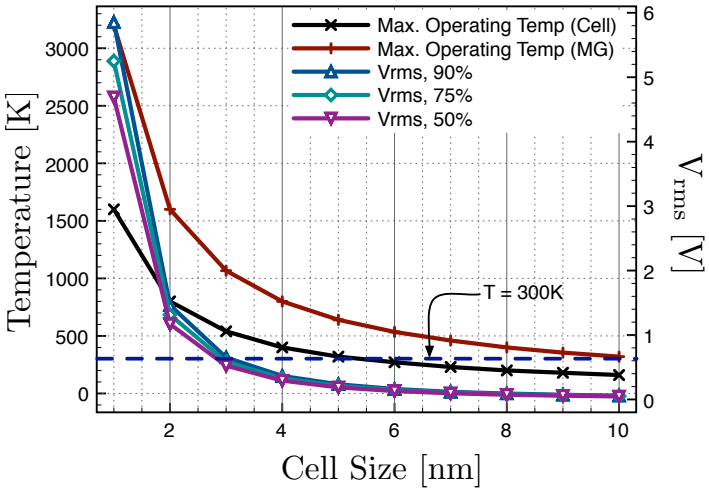

Figure 25. Maximum operating temperature for two neighboring cells and MG configuration 1 as a function of the cell size. The maximum RMS voltages are also shown for varying percentages of charge in the upper and lower sites of the cell.

Figure 25 highlights the trade-offs that exist between the cell size, switching potential and maximum operating temperature. While increasing cell size can significantly reduce the V_{rms} required, this comes at the expense of lower operating temperature. From Figure 25, to operate at room temperature, a cell size no larger than 6 nm and an RMS voltage of approximately 0.163 V is required to ensure that at least 90% of the charge is driven to the upper and lower sites.

11. Conclusion

A simplified model of a molecular QCA cell was investigated in order to develop analytical expressions for the energies associated with the ACTIVE, NULL and X states of a QCA cell. Furthermore, we established limitations on the applied potential and phase of the clocking electrodes to ensure error-free operation of fundamental building blocks in a QCA circuit. It was found that the required potentials on the clocking electrodes are limited by the majority gate and are highly dependent on the cell dimensions and position of the counter-ion charge. It was also found that the electrode potentials needed to drive a cell into one of the unwanted X states was far greater than the potentials required to switch the majority gate and as such, require no additional design considerations. The limits presented in our paper will serve to aid in the selection of molecular structures. In addition, the proper design of appropriate

molecular structures and of the clocking electrodes will reduce the power consumption of the underlying clocking distribution network. We have also shown that there exists a trade-off between the required switching potential, cell size, and operating temperature. As the cell size is decreased, room temperature operation is possible but the minimum potential required to switch a cell from an ACTIVE to a NULL state is increased. Increasing the cell size decreases the minimum switching potential, however, the ability of cells to fully polarize is limited by thermal fluctuations. The results also provide additional evidence that molecular QCA circuits are able to be clocked with reasonable potentials and operate at room temperature, adding further motivation to realize such circuits. The model and methodology presented in this work significantly reduces the computational time required to model the energetics of large QCA systems and can be used to estimate *a priori* the RMS voltages required to clock the circuits.

Acknowledgments

The authors wish to acknowledge helpful discussions with Prof. Alireza Nojeh, and the financial support from the University of British Columbia, as well as the Natural Science and Engineering Research Council of Canada (NSERC), Micronet R&D, the Canadian Foundation for Innovation (CFI), and the British Columbia Knowledge Development Fund (BCKDF).

Appendix

A. Maximum Phase Difference

Let the potentials on two neighboring electrodes, phase-shifted by ϕ, be

$$V_1 = V_0 \cos(\omega t), \tag{A-1}$$

$$V_2 = V_0 \cos(\omega t + \phi), \tag{A-2}$$

such that their difference in potential is,

$$\Delta V_e = V_2 - V_1 \tag{A-3}$$

$$= 2V_0 \sin(\frac{\phi}{2}) \sin(\frac{\phi}{2} + \omega t) \tag{A-4}$$

Next, find the time at which ΔV_e is at a maximum, *i.e.*, solve

$$\frac{d}{dt}\Delta V_e = 0 \tag{A-5}$$

for t. Equation (A-5) gives,

$$t = \frac{\pm\pi - \phi}{2\omega}. \tag{A-6}$$

Inserting this t into equation (A-4) yields,

$$\Delta V_e = \pm 2V_0 \sin(\frac{\phi}{2}). \tag{A-7}$$

Solving for ϕ, we get

$$\phi_{max} = \pm 2 \sin^{-1}(\frac{\Delta V_{e_{max}}}{2V_0}). \tag{A-8}$$

B. Inter-cellular Energy: Wire

For Wire configuration 1, we express the interaction energies as,

$$\begin{aligned} U^{inter_{(w1)}}_{NULL,\kappa_m} &= \sum_{i=0}^{5} Q^n_{NULL}(i) V^{n+1}_{\kappa_{n+1}}(i) \\ &\quad + \sum_{i=0}^{5} Q^n_{NULL}(i) V^{n-1}_{\kappa_{n-1}}(i) \\ &= \sum_{i=0}^{5} Q^n_{NULL}(i) V^{n+1}_{ACTIVE}(i) \\ &\quad + \sum_{i=0}^{5} Q^n_{NULL}(i) V^{n-1}_{ACTIVE}(i) \end{aligned} \tag{B-1}$$

$$\begin{aligned} U^{inter_{(w1)}}_{ACTIVE,\kappa_m} &= \sum_{i=0}^{5} Q^n_{ACTIVE}(i) V^{n+1}_{\kappa_{n+1}}(i) \\ &\quad + \sum_{i=0}^{5} Q^n_{ACTIVE}(i) V^{n-1}_{\kappa_{n-1}}(i) \\ &= \sum_{i=0}^{5} Q^n_{ACTIVE}(i) V^{n+1}_{ACTIVE}(i) \\ &\quad + \sum_{i=0}^{5} Q^n_{ACTIVE}(i) V^{n-1}_{ACTIVE}(i), \end{aligned} \tag{B-2}$$

However, due to symmetry, equations (B-1) and (B-2) reduce to,

$$U^{inter_{(w1)}}_{NULL,\kappa_m} = 2 \sum_{i=0}^{5} Q^n_{NULL}(i) V^{n+1}_{ACTIVE}(i), \tag{B-3}$$

$$U^{inter_{(w1)}}_{ACTIVE,\kappa_m} = 2 \sum_{i=0}^{5} Q^n_{ACTIVE}(i) V^{n+1}_{ACTIVE}(i). \tag{B-4}$$

The difference in state energies becomes,

$$\Delta U^{inter_{(w1)}}_{NA} = U^{inter_{(w1)}}_{NULL,\kappa_m} - U^{inter_{(w1)}}_{ACTIVE,\kappa_m}. \tag{B-5}$$

The same derivation can be applied to find the interaction energies for Wire configuration 2.

C. Intercellular Energy: Majority Gate

For MG configuration 1, we can express the interaction energies as,

$$\begin{aligned} U^{inter_{(mg1)}}_{NULL,\kappa_m} = & \sum_{i=0}^{5} Q^1_{NULL}(i)V^2_+(i) \\ & + \sum_{i=0}^{5} Q^1_{NULL}(i)V^3_-(i) \\ & + \sum_{i=0}^{5} Q^1_{NULL}(i)V^4_+(i) \\ & + \sum_{i=0}^{5} Q^1_{NULL}(i)V^5_+(i), \end{aligned} \tag{C-1}$$

$$\begin{aligned} U^{inter_{(mg1)}}_{ACTIVE,\kappa_m} = & \sum_{i=0}^{5} Q^1_+(i)V^2_+(i) + \sum_{i=0}^{5} Q^1_+(i)V^3_-(i) \\ & + \sum_{i=0}^{5} Q^1_+(i)V^4_+(i) + \sum_{i=0}^{5} Q^1_+(i)V^5_+(i). \end{aligned} \tag{C-2}$$

However, due to the symmetry of the majority gate, we can simplify equations (C-1) and (C-2) such that,

$$\begin{aligned} U^{inter_{(mg1)}}_{NULL,\kappa_m} = & 2\sum_{i=0}^{5} Q^1_{NULL}(i)V^2_+(i) \\ & + \sum_{i=0}^{5} Q^1_{NULL}(i)V^3_-(i) \\ & + \sum_{i=0}^{5} Q^1_{NULL}(i)V^5_+(i), \end{aligned} \tag{C-3}$$

$$\begin{aligned} U^{inter_{(mg1)}}_{ACTIVE,\kappa_m} = & 2\sum_{i=0}^{5} Q^1_+(i)V^2_+(i) + \sum_{i=0}^{5} Q^1_+(i)V^3_-(i) \\ & + \sum_{i=0}^{5} Q^1_+(i)V^5_+(i). \end{aligned} \tag{C-4}$$

The difference in state energies becomes,

$$\Delta U^{inter_{(mg1)}}_{NA} = U^{inter_{(mg1)}}_{NULL,\kappa_m} - U^{inter_{mg1}}_{ACTIVE,\kappa_m}. \tag{C-5}$$

The same derivation can be applied to find the interaction energies for MG configuration 2.

[1] C. S. Lent, P. D. Tougaw, W. Porod, and G. H. Bernstein. Quantum cellular automata. *Nanotechnology*, 4:49–57, 1993.

[2] Y. Lu and C. S. Lent. Theoretical Study of Molecular Quantum-dot Cellular Automata. *J. Comput. Elec.*, 4:115–118, 2005.

[3] C. S. Lent, B. Isaksen, and M. Lieberman. Molecular quantum-dot cellular automata. *J. Am. Chem. Soc.*, 125:1056–1063, 2003.

[4] J. Jiao, G. J. Long, F. Grandjean, A. M. Beatty, and T. P. Fehlner. Building blocks for the molecular expression of quantum cellular automata. isolation and characterization of a covalently bonded square array of two ferrocenium and two ferrocene complexes. *J. Am. Chem. Soc.*, 125(25):7522–7523, 2003.

[5] C. S. Lent and B. Isaksen. Clocked molecular quantum-dot cellular automata. *IEEE Trans. Electron Devices*, 50(9):1890–1896, 2003.

[6] Z. Jin. Fabrication and measurement of molecular quantum cellular automata (QCA) device. Master's thesis, University of Notre Dame, Notre Dame, IN 46556, 2006.

[7] Z. Li and T. P. Fehlner. Molecular QCA cells. 2. characterization of an unsymmetrical dinuclear mixed-valence complex bound to a au surface by an organic linker. *Inorg. Chem.*, 42(18):5715–5721, 2003.

[8] Z. Li, A. M. Beatty, and T. P. Fehlner. Molecular QCA cells. 1. structure and functionalization of an unsymmetrical dinuclear mixed-valence complex for surface binding. *Inorg. Chem.*, 42(18):5707–5714, 2003.

[9] H. Qi, S. Sharma, Z. Li, G. L. Snider, A. O. Orlov, C. S. Lent, and T. P. Fehlner. Molecular quantum cellular automata cells. electric field driven switching of a silicon surface bound array of vertically oriented two-dot molecular quantum cellular automata. *J. Am. Chem. Soc.*, 125(49):15250–15259, 2003.

[10] M. Macucci, M. Gattobigio, L. Bonci, G. Iannaccone, F. E. Prins, C. Single, G. Wetekam, and D. P. Kern. A QCA cell in silicon-on-insulator technology: theory and experiment. *Superlattices Microstruct.*, 34(3):205–211, September 2004.

[11] A. O. Orlov, R. K. Kummamuru, R. Ramasubramaniam, C. S. Lent, G. H. Berstein, and G. L. Snider. Clocked quantum-dot cellular automata shift register. *Surf. Sci.*, 532–535:1193–1198, 2003.

[12] I. Amlani, A. O. Orlov, G. Toth, G. H. Bernstein, C. S. Lent, and G. L. Snider. Digital logic gate using quantum-dot cellular automata. *Science*, 284:289–291, April 1999.

[13] I. Amlani, A. O. Orlov, G. L. Snider, and C. S. Lent. Demonstration of a functional quantum-dot cellular automata cell. *J. Vac. Sci. Technol. B*, 16:3795–3799, 1998.

[14] C. S. Lent, G. L. Snider, G. H. Bernstein, W. Porod, A. O. Orlov, M. Lieberman, T. Fehlner, M.T. Niemier, and P. Kogge. *Quantum-Dot Cellular Automata.* Kluwer Academic Publishers, Boca Raton, FL, USA, 2003.

[15] G. L. Snider, I. Amlani, A. O. Orlov, G. Toth, G. Bernstein, C. S. Lent, J. L. Merz, and W. Porod. Quantum-dot cellular automata: Line and majority gate logic. *Jpn. J. of Applied Physics*, 38:7227–7229, 1999.

[16] R.V. Kummamuru, J. Timler, G. Toth, C. S. Lent, R. Ramasubramaniam, A. O. Orlov, and G. H. Bernstein. Power gain and dissipation in a quantum-dot cellular automata latch. *Appl. Phys. Letters*, 81:1332–1334, 2002.

[17] G. Toth and C. S. Lent. Quasiadiabatic switching of metal-island quantum-dot cellular automata. *J. Appl. Phys.*, 85(5):2977–2984, 1999.

[18] A. Imre and G. Csaba and L. Ji and A. O. Orlov and G. H. Bernstein and W. Porod. Majority Logic Gate for Magnetic Quantum-Dot Cellular Automata. *Science*, 311(5758):205–208, 2006.

[19] C. György *et al.* Nanocomputing by field-coupled nanomagnets. *IEEE Trans. Nano.*, 1(4):209–213, 2002.

[20] C. György and W. Porod. Simulation of field coupled computing architectures based on magnetic dot arrays. *J. Comp. Elec.*, 1(1):87–91, 2002.

[21] M. C. B. Parish. *Modeling of Physical Constraints on Bistable Magnetic Quantum Cellular Automata*. PhD thesis, University of London, 2003.

[22] M. E. Welland R. P. Cowburn. Room temperature magnetic quantum cellular automata. *Science*, 287:1466–1468, 2000.

[23] G. H. Bernstein, A. Imre, V. Metlushko, L. Ji, A. O. Orlov, G. Csaba, and W. Porod. Magnetic QCA Systems. *Microelectronics Journal*, 36:619–624, 2005.

[24] M. Haider et. al. Controlled coupling and occupation of silicon atomic quantum dots at room temperature. *Phys. Rev. Let.*, 102, 2009.

[25] K. Walus and G. A. Jullien. Design tools for an emerging SoC technology: quantum-dot cellular automata. *Proc. IEEE*, 94(6):1225–1244, June 2006.

[26] K. Walus, T. Dysart, G. A. Jullien, and R. A. Budiman. QCADesigner: A rapid design and simulation tool for quantum-dot cellular automata. *IEEE Trans. Nano.*, 3(1):26–31, March 2004.

[27] K. Walus, R. A. Budiman, and G. A. Jullien. Split current quantum dot cellular automata - modeling and simulation. *IEEE Trans. Nano.*, 3(2):249–255, June 2004.

[28] K. Walus and G. Schulhof. QCADesigner Homepage. *[Online] http://www.qcadesigner.ca/*, 2001.

[29] K. Walus, M. Mazur, G. Schulhof, and G. A. Jullien. Simple 4-bit processor based on quantum-dot cellular automata (QCA). In *Proc. of Application Specific Architectures, and Processors Conference*, pages 288–293, July 2005.

[30] K. Walus, G. Schulhof, R. Zhang, W. Wang, and G. A. Jullien. Circuit design based on majority gates for applications with quantum-dot cellular automata. In *Proc. of IEEE Asilomar Conference on Signals, Systems, and Computers*, November 2004.

[31] K. Walus, G. Schulhof, and G. A. Jullien. High level exploration of quantum-dot cellular automata (QCA). In *Proc. of IEEE Asilomar Conference on Signals, Systems, and Computers*, November 2004.

[32] K. Hennessy and C. S. Lent. Clocking of molecular quantum-dot cellular automata. *J. Vac. Sci. Technol. B*, 19(5):1752–1755, 2001.

[33] E. P. Blair and C. S. Lent. An architecture for molecular computing using quantum-dot cellular automata. In *Proc. of the Third IEEE Conference on Nanotechnology*, pages 402–405, 2003.

[34] E. P. Blair. Tools for the design and simulation of clocked molecular quantum-dot cellular automata circuits. Master's thesis, University of Notre Dame, Notre Dame, IN 46556, 2003.

[35] Data flow in molecular QCA: Logic can "sprint," but the memory wall can still be a "hurdle". 2005.

[36] J. Timler and C. S. Lent. Power gain and dissipation in quantum-dot cellular automata. *J. Appl. Phys.*, 91(2):823–831, January 2002.

[37] C. Lent, M. Liu, and Y. Lu. Bennett clocking of quantum-dot cellular automata and the limits to binary logic scaling. *Nanotechnology*, 17(16):4240–4251, 2006.

[38] K Walus, R A Budiman, and G A Jullien. Impurity charging in semiconductor quantum-dot cellular automata. *Nanotechnology*, 16(11):2525–2529, 2005.

[39] K. Walus. *Design and Simulation of Quantum-Dot Cellular Automata Devices and Circuits*. PhD thesis, University of Alberta, September 2005.

[40] Z. Li and M. Lieberman. Axial reactivity of soluble silicon(IV) phthalo-cyanines. *Inorg. Chem.*, 40:932–939, 2001.

[41] K.D. Demadis, C.M. Hartshorn, and T.J. Meyer. The localized-to-de-localized transition in mixed-valence chemistry. *Chem. Rev.*, 101:2655–2685, 2001.

[42] Y. Lu, Mo Liu and C. S. Lent. Molecular electronics - from structure to dynamics. In *Proc. of the Sixth IEEE Conference on Nanotechnolgy*, 2006.

[43] Y. Lu, Mo Liu and C. S. Lent. Molecular quantum-dot cellular automata: From structure to dynamics. *J. App. Phys.*, 102, 2007.

[44] Y. Lu and C. Lent. A metric for characterizing the bistability of molecular quantum-dot cellular automata. *Nanotechnology*, 19, 2008.

[45] C. S. Lent. "Re: QCA Related Questions." E-mail to Konrad Walus. 11 November 2008.

[46] C. S. Lent and Beth Isaksen. Clocked Molecular Quantum-Dot Cellular Automata. *IEEE Trans. on Electron Dev.*, 50:1890–1896, 2003.

[47] M. Sadiku. *Elements of electromagnetics, 3rd Ed.* Oxford University Press, USA, 1994.

[48] K. W. Whites C. R. Paul and S. A. Nasar. *Introduction To Electromagnetic Fields, 3rd Ed.* McGraw-Hill, Cambridge, Massachusetts, 1998.

[49] A. Nojeh, A. Ural, R. F. Pease, and H. Dai. Electric-field-directed growth of carbon nanotubes in two dimensions. *J. Vac. Sci. Technol. B*, 22(6):3421–3425, 2004.

[50] P. Visconti, A. Della Torre, G. Maruccio, E. D'Amone, A. Bramanti, R. Cingolani, and R. Rinaldi. The fabrication of sub-10nm planar electrodes and their use for a molecule-based transistor. *Institute of Physics Publishing: Nanotechnology*, 15:807–811, 2004.

[51] K. Liu, Ph. Avouris, J. Bucchignano, R. Martel, S. Sun, , and J. Michi. Simple fabrication scheme for sub-10 nm electrode gaps using electron-beam lithography. *Applied Physics Letters*, 5(80):865–867, 2002.

[52] M. Macucci, G. Iannaccone, S. Francaviglia, and B. Pellegrini. Semiclassical simulation of quantum cellular automaton circuits. *Int. J. Cir. Theor. Appl.*, 29(1):37–47, January 2001.

[53] C. Ungarelli, S. Francaviglia, M. Macucci, and G. Iannaccone. Thermal behavior of quantum cellular automaton wires. *Journal of Applied Physics*, 87(10):7320–7325, 2000.